



Resistance Spot Welding of Aluminum Alloy to Steel with Transition Material — Part II: Finite Element Analyses of Nugget Growth

An aluminum-clad steel transition layer can be used in forming a structural weld between aluminum and steel parts

BY X. SUN AND M. A. KHALEEL

ABSTRACT. This paper summarizes work on finite element modeling of nugget growth for resistance spot welding of aluminum alloy to steel. It is a sequel to a previous paper on experimental studies of resistance spot welding of aluminum to steel using a transition material. Since aluminum alloys and steel cannot be readily fusion welded together due to their drastically different thermal physical properties, a cold-rolled clad material was introduced as a transition to aid the resistance welding process. Coupled electrical-thermal-mechanical finite element analyses were performed to simulate the nugget growth and heat generation patterns during the welding process. The predicted nugget growth results were compared to the experimental weld cross sections. Reasonable comparisons of nugget size were achieved. The finite element simulation procedures were also used in the electrode selection stage to help reduce weld expulsion and improve weld quality.

Introduction

Steel and aluminum are the most important construction materials for the mass production of today's automotive structures. It is well known that metallurgical bonds between aluminum and steel are difficult to achieve with fusion welding because of the inherent discrepancies in electrical, thermal, and mechanical properties between the two materials. For fusion welding processes such as direct resistance spot welding (RSW), little or no mutual solubility of aluminum and steel exists. The intermetallic compound that is

formed between the two metals often results in cracking, brittleness, and susceptibility to corrosion. The use of a transition material to facilitate the spot welding process of aluminum to steel is a concept that has shown promise in the past (Refs. 1, 2). Use of this transition insert allows for two separate weld nuggets to be formed in their respective aluminum/aluminum and steel/steel interfaces. Bonding at the aluminum/steel interface is achieved by the cold-clad process (Ref. 1).

Very few previous studies exist on this subject matter, and almost all of these studies focus on experimental nugget growth studies using consecutive metallurgical cross-sectioning. There is a lack of fundamental understanding on the heat generation and nugget growth kinetics as well as the effects of different electrode combinations on nugget growth kinetics. The purpose of this study was to use the incrementally coupled finite element modeling procedure to simulate the heat generation and nugget formation sequence in resistance welding of aluminum to steel with a transition layer. As discussed in Part I of this study, the transition layer used was a cold-rolled clad material of aluminum to steel with 20% cladding ratio. The process development and joint performance issues were addressed in Part

I of this study using experimental approaches. The following welding parameters were used for spot welding of 2-mm 5182-O to 1.4-mm SAE1008 with 1.5-mm-thick transition material:

- Electrode on Al side: 30-deg truncated cone Class 2 electrode with 8-mm face diameter and 3-in. face radius
- Electrode on steel side: 30-deg truncated cone Class 2 electrode with 8-mm diameter, flat-faced
- Electrode force: 1050 lb-ft.
- Welding current: 13.6 kA with 97% heat
- Welding schedule: 3 pulses of [12 cycles welding + 3 cycles holding]
- Cooling water flow rate: 1.75 gallons per min

With the rapid advancements in software and hardware for scientific computing, finite element weld process simulation has been a powerful tool in understanding the fundamental physics associated with the resistance spot welding process. Several authors have developed different finite element models to address various aspects associated with the resistance spot welding process. Among them are Nied (Ref. 3), Tsai et al. (Ref. 4), Sheppard (Ref. 5), Murakawa (Ref. 6), and Dong et al. (Ref. 7). Most of the above-mentioned studies use sequentially coupled finite element modeling in which a one-step electrical-thermal analysis is performed after the initial mechanical analysis of the holding cycle. No changes in contact areas between the electrode and worksheet are monitored and updated during the modeling process.

During actual welding, however, the contact area changes on the faying interface and the two electrode/sheet interfaces can significantly influence the heat

KEY WORDS

Welding Process Simulation
Finite Element Analysis
Resistance Spot Welding
Dissimilar Metals Joining
Aluminum Alloy
Transition Material
Aluminum-Clad Steel
Nugget Growth

X. SUN is with Battelle Memorial Institute, Columbus, Ohio. M. A. KHALEEL is with Pacific Northwest National Laboratory, Richland, Wash.

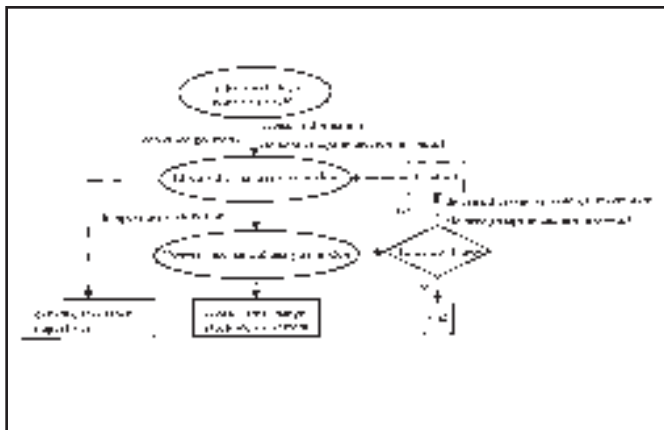


Fig. 1 — Flowchart of analysis procedure.

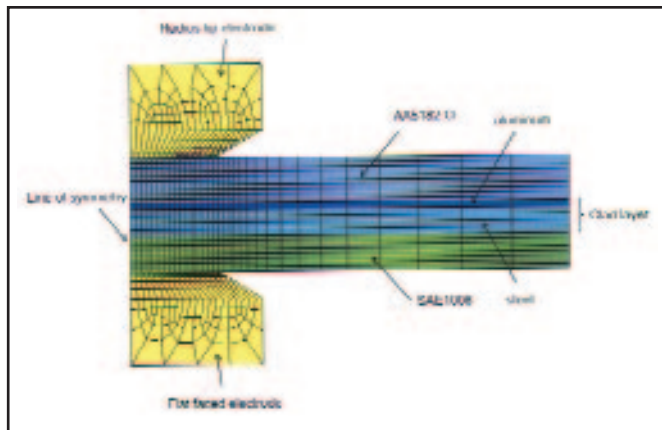


Fig. 2 — Typical finite element mesh.

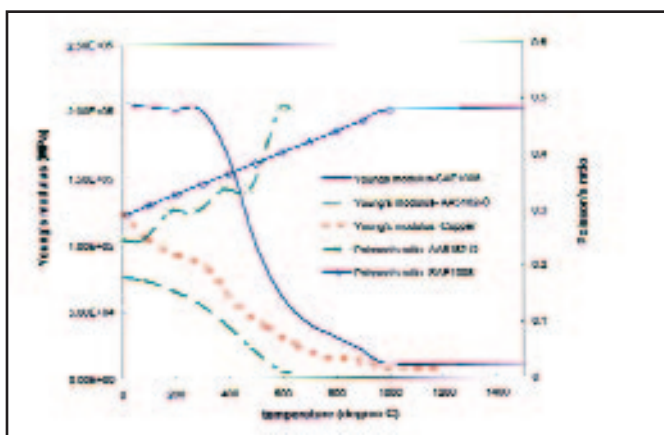


Fig. 3 — Young's modulus and Poisson's ratio of different materials.

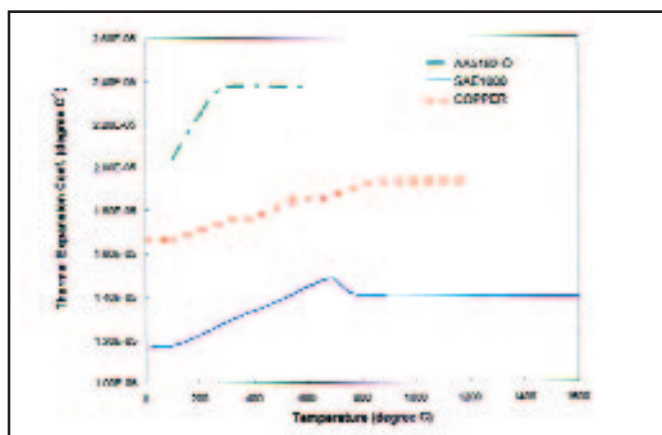


Fig. 4 — Thermal expansion coefficient of different materials.

generation and nugget formation processes (Ref. 8). This is particularly true for aluminum spot welding with radius-tip electrodes. In this study, we used the incrementally coupled finite element procedure developed by Sun and Dong (Ref. 9) to simulate the nugget growth and heat generation process for resistance spot welding of aluminum to steel. The theoretical framework regarding the coupled electrical-thermal-mechanical phenomena associated with spot welding was presented in Ref. 9 and its implementation procedure with commercial code (e.g., *ABAQUS*) is illustrated in Fig. 1. This incrementally coupled modeling procedure has been proven successful in modeling aluminum spot welding and steel projection welding processes (Refs. 9–11).

Finite Element Modeling Procedure

Figure 2 shows the typical finite element mesh for half of the electrode-sheet assembly with axisymmetric condition being assumed. The 2-mm AA5182-O is

in contact with the top electrode and the aluminum side of the transition clad layer. The 1.4-mm SAE1008 sheet is in contact with the bottom electrode and the steel side of the transition layer. The total thickness of the transition material is 1.5 mm. The model consists of four-node linear elements.

The initial squeeze cycle is modeled by a mechanical analysis. Uniformly distributed pressure calculated according to the specified electrode force is applied on the top surface of the upper electrode, and the bottom of the lower electrode is restrained from motion in the vertical direction. Contact pairs are set up for the electrode/sheet interfaces and the two faying interfaces to model surface interactions (Refs. 9, 12). Results generated from the squeezing cycle mechanical analysis, including deformed shape and coordinates, contact pressure, contact radius, element groups in and not in contact, etc., are extracted and passed to the subsequent electrical-thermal analysis in which the welding current is applied. Temperature-dependent mechanical properties are used for

AA5182-O and SAE1008, as well as the copper electrodes. These data are collected from various references (Refs. 13–16). For example, Figs. 3 and 4 show the temperature-dependent Young's modulus, Poisson's ratio, and thermal expansion coefficient for the different materials used in the analyses. Note that the material properties for the aluminum and steel layers in the transition material are assumed to be the same as AA5182-O and SAE1008, respectively.

In the electrical-thermal analysis, the deformed shape of the electrode-sheet assembly calculated from the previous mechanical analysis is used. Zero electrical potential is imposed on the bottom of the lower electrode tip, and distributed current density input calculated from the current input value is applied on the top of the upper electrode. All the free surfaces of the electrode and sheet assembly that are not in contact at this time increment are assumed to have free convection with the surrounding air, and the two electrodes are assumed to be water cooled with a forced-convection coefficient spec-

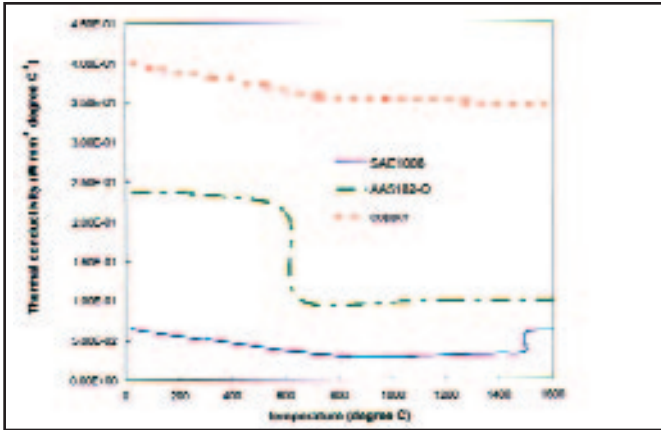


Fig. 5 — Thermal conductivity of different materials.

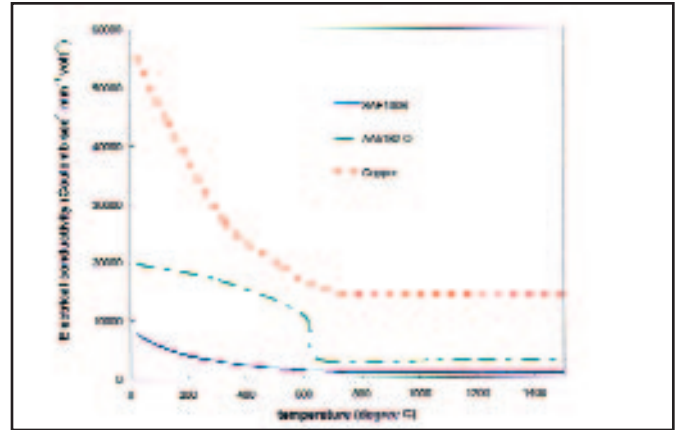


Fig. 6 — Electrical conductivity of different materials.

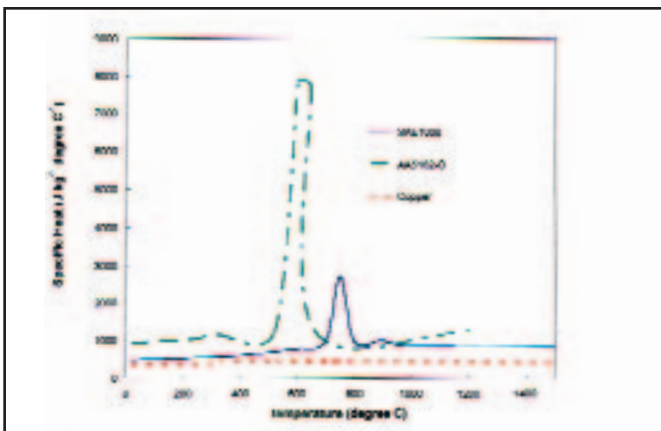


Fig. 7 — Specific heat of different materials.

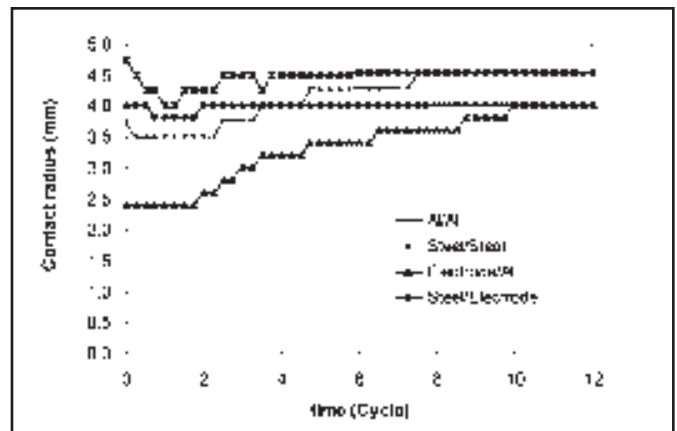


Fig. 8 — Predicted evolution of contact radii on different interfaces during the first welding pulse.

ified on their upper and lower free edges. Figures 5–7 show the temperature-dependent physical properties used for the materials during the entire modeling process (Refs. 13–16).

The contact electrical conductance for the faying interfaces and the electrode/sheet interfaces is determined using the formulation developed by Li et al. (Ref. 8):

$$\sigma_g = \frac{1}{\rho h} = \frac{1}{R_c A_c} = \frac{I}{2\sqrt{L(T_s^2 - T_0^2)}\pi r_c^2} \quad (1)$$

in which L is the Lorentz constant; T_s is the solidus temperature of the interface; and T_0 is the interface temperature (both in Kelvin). For most metals, L is found to be around $2.4 \times 10^{-8} (V/^\circ K)^2$. The contact radius r_c for the electrode-sheet interfaces and the faying interface is extracted from the previous increment mechanical analysis results. The solidus temperatures T_s for different interfaces used in the analyses are

$$\begin{aligned} T_{s\text{-electrode/aluminum}} &= 200^\circ\text{C} \\ T_{s\text{-aluminum/aluminum}} &= 550^\circ\text{C} \\ T_{s\text{-steel/steel}} &= 1200^\circ\text{C} \\ T_{s\text{-electrode/steel}} &= 500^\circ\text{C} \end{aligned}$$

The temperature distribution computed from the above electrical-thermal analysis for a certain time increment is then imposed as thermal loading conditions for the subsequent thermal-mechanical analysis module. This updating procedure repeats itself for a specific time increment, i.e., the updating frequency, until the entire welding cycle is totally completed. The flowchart of the analysis procedure is shown in Fig. 1. The entire analysis procedures are fully automated with a suite of user-interface routines.

Results and Discussions

Nugget Development Study

The modeling procedure described above was used to simulate the RSW process of aluminum to steel with transi-

tion clad material. In the coupled finite element analyses, the updating frequency for the first welding pulse (12 cycles of welding current) was set to be $\frac{1}{4}$ cycle to capture the rapid changes of the contact radii on different interfaces as depicted in Fig. 8. Toward the end of the first welding pulse, the contact radii on different interfaces reached their respective plateaus, then single-step thermal-electrical analyses were performed for the subsequent second and third welding pulses.

The predicted nugget shape and size compared with the weld cross sections from the actual weld samples are shown in Figs. 9–13. It should be mentioned that since aluminum and steel have different melting temperatures, different contour scales had to be used in plotting the temperature contours of the model prediction in order to show molten zones in both aluminum and steel in one picture. In Figs. 9–13, the red areas in the predicted results represent molten metal, and the gray areas in the predicted results represent base material: light gray for aluminum and dark gray for steel. The sharp transition

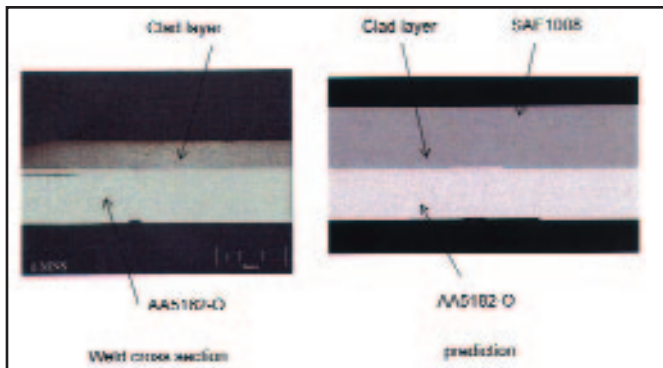


Fig. 9 — Weld structure at four cycles weld time: no melting observed. The steel sheet separated from the transition clad layer due to short weld time.

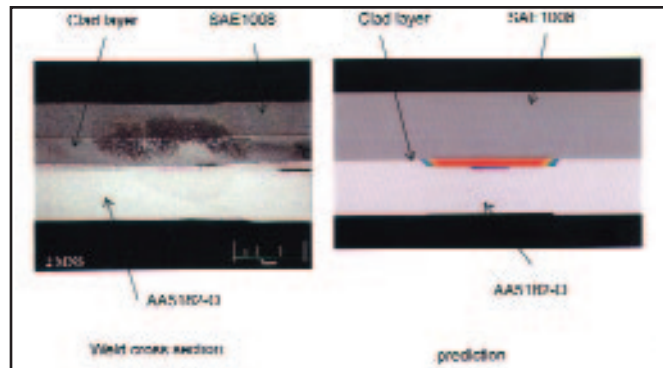


Fig. 10 — Weld structure at eight cycles weld time.

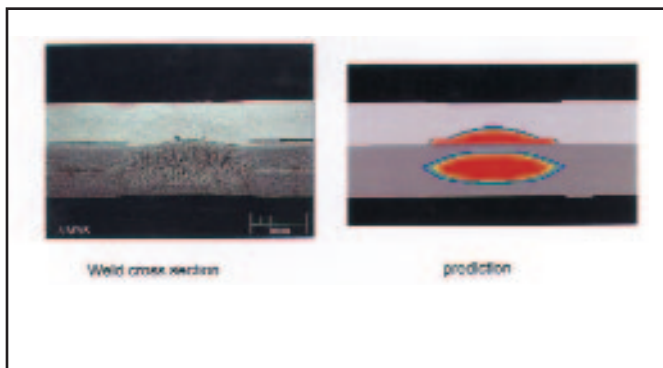


Fig. 11 — Weld structure at 12 cycles weld time (first pulse).

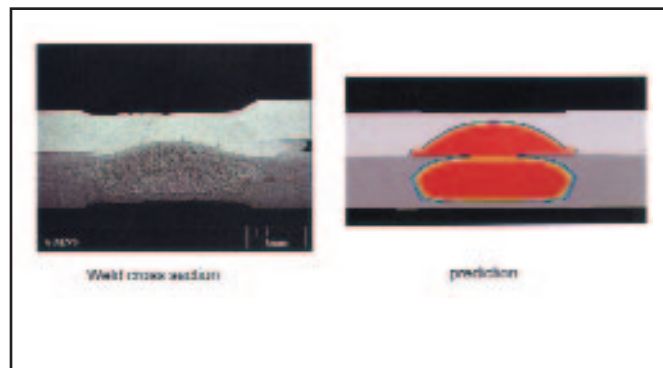


Fig. 12 — Weld structure at the end of the second welding pulse.

regions between the base material and the molten zone are the predicted heat-affected zone (HAZ). Furthermore, in order to show the model predicted fusion zone size and shape, Figs. 9–13 were plotted at the end of the welding cycles, not at the end of the holding and cooling cycles as those in the experimental cross sections. Since the materials are still hot at the end of the welding cycle and are still undergoing thermal expansions, these temperature contour plots can only be used to determine the fusion zone width and its depth relative to the original sheeting thickness. They do not represent the final weld indentation and sheet separation. This is particularly true for the softer aluminum side, where large deformation will occur during the cooling and holding cycle. And it explains why the contour plots in Figs. 9–13 do not show significant weld deformations as shown in the experimental cross sections.

Figures 9–11 show the molten zone formation sequence for the first welding pulse (12 welding cycles). At the end of the first four welding cycles, no melting is predicted, neither on the aluminum side nor on the steel side. This is consistent with the experimental observations in Fig. 9. At the end of the eighth welding cycle, a small amount of

melting is predicted on the aluminum side of the transition material in Fig. 10. This melting is caused primarily by the heat conducted from the steel/steel interface. Since the melting temperature for steel is much higher than aluminum, melting is not yet observed for the steel side at the end of the eighth cycle. Some discoloration is observed on the steel/steel interface in the metallurgical cross section in Fig. 10 with no clear columnar weld structure present. This discoloration could be the result of recrystallization, grain growth, and re-austenization of the material. The maximum temperature predicted for the steel/steel faying interface at the end of the eighth welding cycle is 1437°C, very close to the melting temperature of steel. The metallurgical cross section in Fig. 10 shows that some amount of melting occurred in the aluminum base material in addition to the aluminum layer in the transition material. Since the steel side of the entire cross section was much hotter than the aluminum side at the end of the eighth cycle, heat from the steel side continued to be conducted to the much cooler aluminum side when the weld current was turned off. This “postweld” heat conduction may cause additional melting on the aluminum side after the current was turned off. Again, since our prediction results are

only depicted at the end of the eighth welding cycle, it does not include any additional melting caused by the heat transfer after the current was turned off. This effect should be particularly strong for the first welding pulse when thermal gradients between the two sides were very high.

At the end of the first welding pulse (12 cycles), both metallurgical cross section and prediction indicated clear molten zones on the steel side as well as the aluminum side — Fig. 11. The molten zone on the steel side has a regular, elliptical shape, with major axis along the interface of the SAE1008 and the steel side of the transition material. Clear dendritic solidification structures surrounded by the heat-affected zone can be observed in the steel nugget. These structures start at the outer edge of the molten nugget and grow like fingers stretching toward the center of the nugget. The molten zone on the aluminum side is only the top half of a regular elliptically shaped spot weld with a slightly larger molten zone diameter in the transition material. This again suggests that the heat for nugget formation on the aluminum side is conducted from the steel side. In addition, pores and gaps were also seen on the aluminum/steel interface. The possible reasons for the pores and gaps to

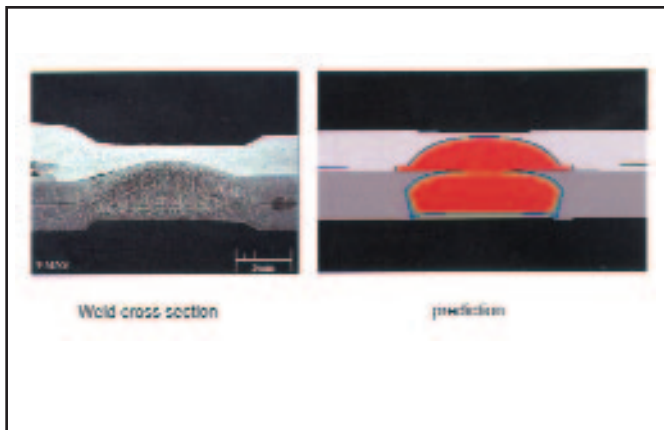


Fig. 13 — Weld structure at the end of the third welding pulse.

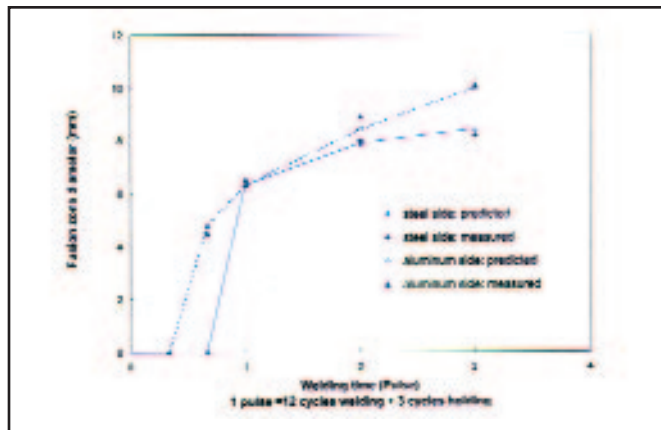


Fig. 14 — Comparison of predicted and measured fusion zone diameter on aluminum/aluminum interface and steel/steel interface.

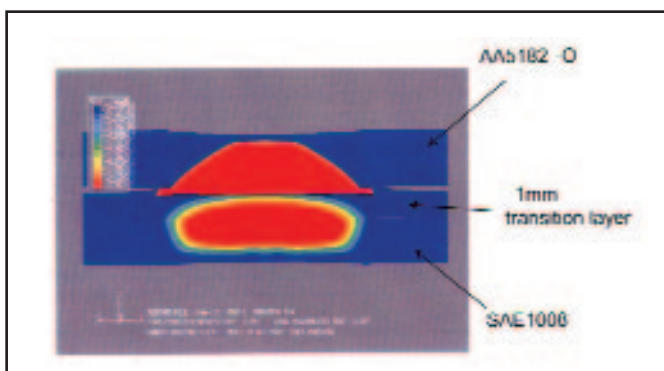


Fig. 15 — Weld structure and sheet separation for radius electrodes on both sides.

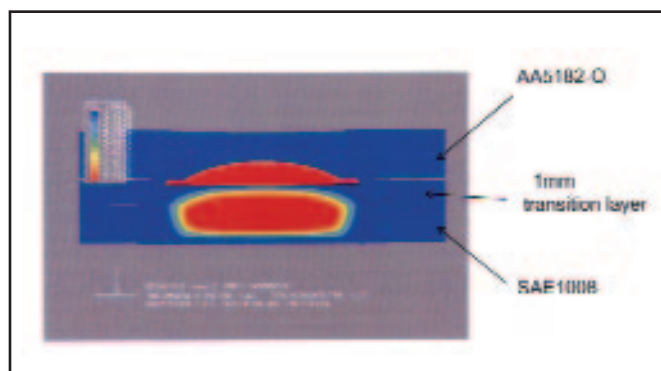


Fig. 16 — Weld structure and sheet separation for radius electrode on aluminum side and flat-faced electrode on steel side.

form were discussed in Part I of our study, and their influence on the weld performance was also discussed. It should be mentioned that the finite element analyses procedure used here cannot be used to predict the formation and location of such pores and gaps.

The predicted weld cross sections at the end of the second and the third welding pulses are shown in Figs. 12 and 13 together with experimental cross sections. Figure 14 compares the predicted and measured fusion zone diameters along the aluminum/aluminum interface and steel/steel interface. Overall, the predicted fusion zone diameters and depths (relative to sheet thickness) are in good comparison with the experimental cross sections on both steel and aluminum sides.

It should be noted that the experimental cross sections shown in Figs. 12 and 13 indicate a large amount of one-sided weld indentation and interface metal squeeze-out. These could be the results of electrode misalignment during the actual welding process. Since the analysis procedures used in this study were based on axisymmetric assumption, the effects of electrode misalignment and one-sided

expulsion were not predicted using the current modeling procedure.

Electrode Selections

As discussed in Part I of this study, during the initial electrode selection stage, the electrode pair first used was based on a Ford specification (Ref. 17) in which 30-deg truncated Class 2 electrodes with 8-mm face diameter and 3-in. face radius were used on both sides. Initial experimental welding trials with this electrode pair resulted in frequent weld expulsion and large sheet separation.

In parallel with the experimental efforts, the coupled finite element modeling procedures described above were also used to study the effects of electrode combinations on the fusion zone size and sheet separation. Figure 15 shows the predicted nugget size and sheet separation with the original electrode pair in which radius-faced weld tips were used on both sides. The welding parameters used in the analyses are also indicated in Fig. 15. It is worth mentioning again that different contour scales were used for the steel and the aluminum sides in generating the contour

plots to illustrate two fusion zones in one picture. In Figs. 15 and 16, the red areas represent the molten metal and the blue areas represent the base metal. The sharp transition regions between these two colors are the heat-affected zone.

The predicted temperature contour and weld deformation show that this electrode combination generates a rather large sheet separation and a much larger fusion zone on the aluminum/aluminum faying interface. As a result of the large fusion zone and sheet separation, there is a lack of contact pressure confinement at the fusion zone periphery, which suggests a strong tendency for expulsion and metal squeeze-out at those locations. This prediction is consistent with the experimental observations from our initial welding trials using this pair of electrodes, where expulsion frequently occurred. In addition, a ring of softened aluminum was observed being squeezed out from the nugget periphery, and it formed a collar of aluminum outside the nugget area on the aluminum/aluminum faying interface, which further aggravated the final sheet separation.

In order to better contain the molten metal on the aluminum side, a larger con-

tact area on the faying interface needed to be established. This was achieved by machining off the radius portion of the electrode tip on the steel side. Using the same welding parameters, the predicted fusion zone size at the end of the welding cycle for this electrode combination is shown in Fig. 16. Compared with the fusion zone shape and contact area at the aluminum/aluminum interface with the results in Fig. 15, this new pair of electrodes offers much larger contact area to contain the molten aluminum and therefore should reduce the occurrence of weld expulsion. Indeed, the experimental welding trials validated this prediction. Therefore, this pair of electrodes with modified electrode tip on the steel side was used for further weld sample fabrication.

Conclusions

The objective of this research was to investigate whether spot welding between aluminum and steel can be achieved using a transition material. Both experimental welding trials and finite element simulations were used in determining the optimal electrode combinations and welding parameters. The nugget formation process was then examined using consecutive metallurgical cross-sectioning and finite element analyses. It was found that two distinct fusion zones formed during the spot welding process of aluminum to steel using a transition aluminum-clad steel strip. The nugget on the steel side is a regular, elliptical weld with dendritic grain structure inside the nugget region. The nugget on the aluminum side is the top half of the elliptical shape. It demonstrated that the incrementally coupled fi-

nite element simulation procedure can be used to study the nugget growth kinetics during the welding process. The analysis procedure was also used in rationalizing the welding test results and in selecting the final electrode combinations for weld coupon fabrication.

Together with the results of Part I of our study, this study suggests that the aluminum-clad steel transition layer can be used in forming a structural weld between aluminum and steel. Moreover, it can be used as a material transition between the aluminum parts and the steel parts of a vehicle to optimize safety and weight reduction of a particular vehicle design.

Acknowledgments

Pacific Northwest National Laboratory is operated by Battelle for the U.S. Department of Energy under Contract DE-AC06-76RL01830. The Department of Energy Office of Transportation Technology funded this work. The DOE program manager is Dr. Joseph Carpenter, and the USCAR program manager is James Quinn.

References

1. Johnson, J., Theile, R., and Kobeloer, N. 2000. Transition material — characteristics of aluminum-clad strip steels. *Proceedings of the IX Sheet Metal Welding Conference*. October, Detroit, Mich.
2. Chang, H. S., Johnson, G. F., Dickinson, D. W., and Tsai, C. L. 1999. Spot welding aluminum to steel — transition material inserts help to overcome incompatibility. *Practical Welding Today*. May/June.
3. Nied, H. A. 1984. The finite element modeling of the resistance spot welding process.

Welding Journal 63(4): 123-s to 132-s.

4. Tsai, C. L., Jammal, O. A., Papritan, C., and Dickinson, D. W. 1992. Modeling of resistance spot weld nugget growth. *Welding Journal* 71(2): 47-s to 54-s. 9.11997. Weldability analysis of spot welding on aluminum using FEM. *Mathematical Modeling of Weld Phenomena*. Ed. H. Cerjak, pp. 944–966. The Institute of Materials.
7. Dong, P., Li, M. V., and Kimchi, M. 1997. Analysis of electrode wear mechanisms: face extrusion and pitting effects. *Science and Technology of Welding and Joining*.
8. Li, M. V., Dong, P., and Kimchi, M. 1997. Modeling of contact resistance during resistance spot welding. *Proc. 7th Int. Conf. on Computer Tech. in Welding*. Ed. T. Siewert, pp. 423–435. NIST Special Publication 923, U.S. Dept. of Commerce.
9. Sun, X., and Dong, P. 2000. Analysis of aluminum resistance spot welding processes using coupled finite element procedures. *Welding Journal* 79(8): 215-s to 221-s.
10. Sun, X. 2001. Effect of projection height on projection collapse and nugget formation — a finite element study. *Welding Journal* 80(9): 211-s to 216-s.
11. Sun, X. 2000. Modeling of projection welding processes using coupled finite element analyses. *Welding Journal* 79(9): 244-s to 251-s.
12. *ABAQUS/Standard* and *ABAQUS/Explicit* user's manuals, Version 6.3. Hibbit, Karlsson & Sorensen, Inc.
13. Properties and selections: irons and steels. 1978. *Metals Handbook*, Ninth Ed., Vol. 1. ASM International, Metals Park, Ohio.
14. Properties and selections: nonferrous alloys and pure metals. 1979. *Metals Handbook*, Ninth Ed., Vol. 2. ASM International, Metals Park, Ohio.
15. *High-Temperature Property Data: Ferrous Alloys*. 1988. Metals Park, Ohio: ASM International.
16. *Physical Constants of Some Commercial Steels at Elevated Temperatures*. 1953. Ed. British Iron and Steel Research Association. London: Butterworth's Scientific Publications.
17. Ford Laboratory Test Method BA 113-07: Welding Acceptance Test for Aluminum.

IIW Annual Assembly Convenes in Japan

The 57th Annual Assembly of the International Institute of Welding (IIW) will be hosted by the Japan Institute of Welding (JIW), at the Osaka International Convention Center, Osaka, Japan, July 11–16, 2004

The IIW is the global body in the science and application of joining technology providing networking and knowledge exchange. Its technical field encompasses the joining, cutting, and surface treatment of metallic and nonmetallic materials by such processes as welding, brazing, soldering, thermal cutting, thermal spraying, adhesive bonding, and microjoining and embraces allied fields including quality assurance, nondestructive testing, standardization, inspection, health and safety, education, training, qualification, design, and fabrication.

The United States will be represented by members of The American Council of the IIW, which is the United States' national committee for the IIW. As a comprehensive forum for professional cooperation through interaction with representatives of the other 41 member countries, the IIW provides a unique opportunity for sharing technological innovations and can be an important avenue for international trade.

For further information on the IIW and membership on The American Council, please contact Andrew Davis, Managing Director, Technical Services Division, at adavis@aws.org, (305) 443-9353, ext. 466; or Gricelda Manalich, IIW Coordinator, at gricelda@aws.org, (305) 443-9353, ext. 294. Further information, including registration forms, can also be obtained from the IIW Secretariat in Paris, France, at www.iiw-iis.org.